

Fault-valve behavior estimated from intensive foreshock and aftershock activity in the 2017 M 5.3 Kagoshima Bay, Kyushu, southern Japan, earthquake sequence

Yoshiaki Matsumoto¹, Keisuke Yoshida¹, Akira Hasegawa¹, and Toru Matsuzawa¹

¹Tohoku University

November 30, 2022

Abstract

Fluid migration and pore pressure changes within the Earth are key to understanding earthquake occurrences. In this study, we investigated the spatiotemporal characteristics of intensive foreshock and aftershock activity for the 2017 M 5.3 earthquake in Kagoshima Bay, southern Japan, to examine the physical process governing this earthquake sequence. We determined that foreshock hypocenters moved slowly on a sharply-defined steeply-dipping plane, which probably represents the same plane of the mainshock source fault. The mainshock hypocenter was located at an edge of a seismic gap formed by foreshocks along the plane, suggesting that the mainshock ruptured this seismic gap. Aftershock hypocenters, distributed along several steeply-dipping planes exhibited an overall upward migration. Aftershock activity slightly deviated from a simple mainshock-aftershock type, suggesting the existence of an aseismic process behind this earthquake sequence. We propose a hypothesis that consistently explains these observations. First, fluids rose from the deeper portion and intruded into the fault plane, reduced the fault strength, and caused the foreshock sequence, as well as, possible aseismic slips. An area with a relatively high fault strength on the plane existed, where the mainshock rupture finally occurred due to a continuous decrease in the fault strength associated with increasing pore pressure and an increase in the shear stress associated with the aseismic slip and foreshocks. The change in the pore pressure associated with post-failure fluid discharge contributed to the aftershock activity, causing upward fluid migration. These observations show the importance of fluid movement at depth, when attempting to understand the earthquake cycle.

1 **Fault-valve behavior estimated from intensive foreshock and aftershock**
2 **activity in the 2017 M 5.3 Kagoshima Bay, Kyushu, southern Japan,**
3 **earthquake sequence**

4 **Yoshiaki Matsumoto¹⁺, Keisuke Yoshida^{1*}, Toru Matsuzawa¹, and Akira Hasegawa¹**

5

6 ¹ Research Center for Prediction of Earthquakes and Volcanic Eruptions, Graduate School of
7 Science, Tohoku University, Sendai 980, Japan

8 + Now at Japan Meteorological Agency, Japan

9

10

11 *Corresponding author: Keisuke Yoshida (keisuke.yoshida.d7@tohoku.ac.jp)

12

13

14

15 **Key Points:**

- 16
- 17 • Intensive foreshock activity exhibits an evident migration behavior on a plane.
 - 18 • Aftershock hypocenters migrate toward shallower levels using several planes.
 - 19 • Upward pore pressure migration explains the occurrence of this foreshock-mainshock-aftershock sequence.

20 **Abstract**

21 Fluid migration and pore pressure changes within the Earth are key to understanding earthquake
22 occurrences. In this study, we investigated the spatiotemporal characteristics of intensive
23 foreshock and aftershock activity for the 2017 M_{JMA} 5.3 earthquake in Kagoshima Bay, southern
24 Japan, to examine the physical process governing this earthquake sequence. We determined that
25 foreshock hypocenters moved slowly on a sharply-defined steeply-dipping plane, which
26 probably represents the same plane of the mainshock source fault. The mainshock hypocenter
27 was located at an edge of a seismic gap formed by foreshocks along the plane, suggesting that
28 the mainshock ruptured this seismic gap. Aftershock hypocenters, distributed along several
29 steeply-dipping planes exhibited an overall upward migration. Aftershock activity slightly
30 deviated from a simple mainshock-aftershock type, suggesting the existence of an aseismic
31 process behind this earthquake sequence. We propose a hypothesis that consistently explains
32 these observations. First, fluids rose from the deeper portion and intruded into the fault plane,
33 reduced the fault strength, and caused the foreshock sequence, as well as, possible aseismic slips.
34 An area with a relatively high fault strength on the plane existed, where the mainshock rupture
35 finally occurred due to a continuous decrease in the fault strength associated with increasing pore
36 pressure and an increase in the shear stress associated with the aseismic slip and foreshocks. The
37 change in the pore pressure associated with post-failure fluid discharge contributed to the
38 aftershock activity, causing upward fluid migration. These observations show the importance of
39 fluid movement at depth, when attempting to understand the earthquake cycle.

40

41 **1. Introduction**

42 Earthquakes are a natural phenomenon wherein a high-speed rupture propagates along a
43 fault. Two factors control the occurrence of an earthquake: an increase in the shear stress acting
44 on the fault and a decrease in the fault strength. Previous studies suggest that an increase in the
45 pore pressure plays an important role in earthquake occurrence (e.g., Hasegawa, 2017; Hubbert
46 & Rubey, 1959; Nur & Booker, 1972; Sibson, 1992; Rice, 1992) because there is a decrease in
47 the fault strength with a rise in the pore pressure.

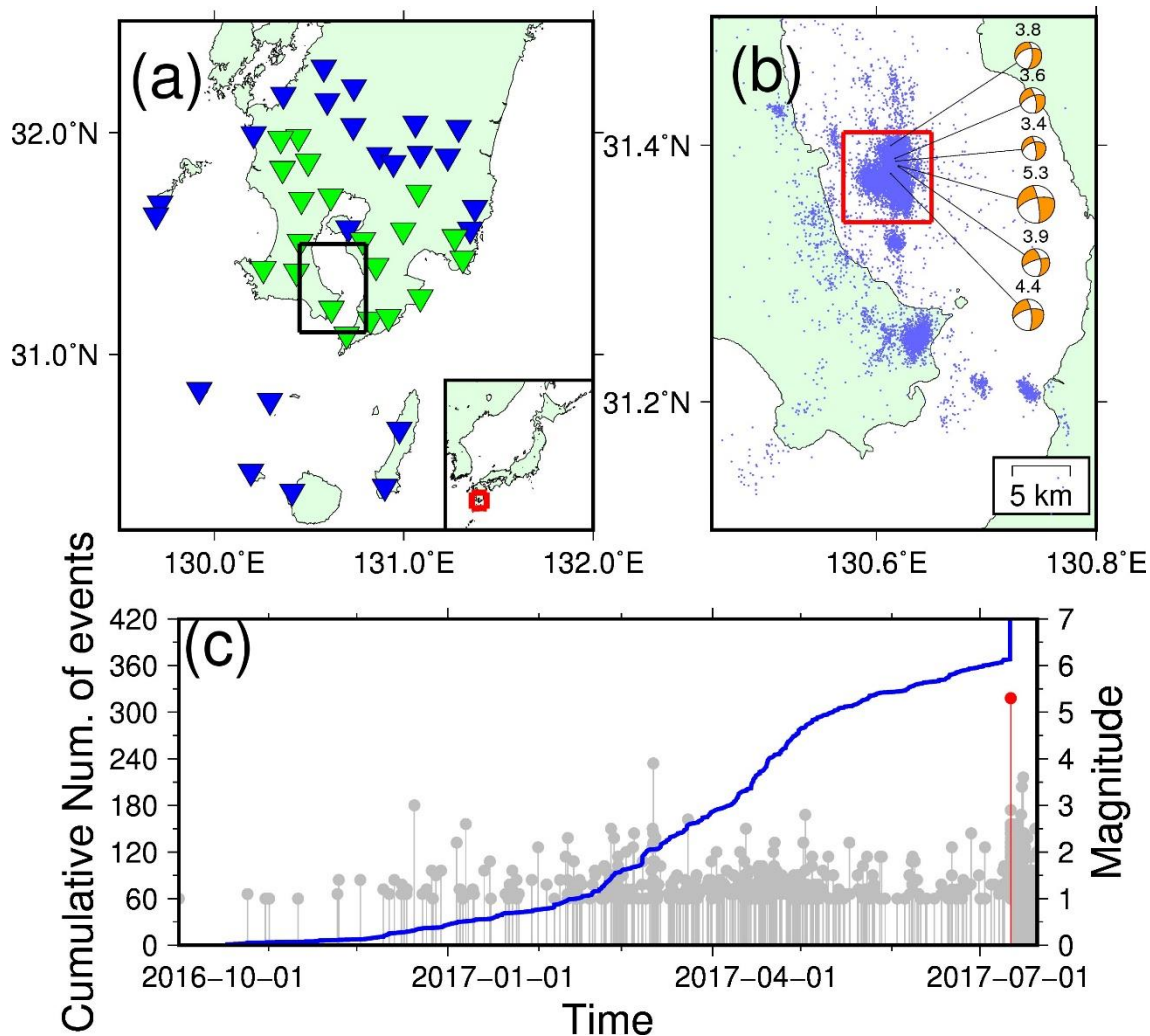
48 A well-known example of fluid-driven seismicity is seismicity induced by fluid injection
49 for engineering purposes (e.g., Ellsworth, 2013). There is also growing evidence that the
50 occurrences of numerous natural earthquake swarms are closely related to fluid movements at
51 depth. Yukutake et al. (2011) precisely determine the hypocenters and focal mechanisms of the
52 2009 Hakone volcano earthquake swarm, suggesting that the diffusion of highly pressured fluid
53 triggered this swarm. Shelly et al. (2016) investigate the spatiotemporal evolution of seismic
54 activity in the Long Valley Caldera, California, suggesting that an evolving pore pressure
55 transient with a low-viscosity fluid initiated and sustained the swarm in 2014. Several earthquake
56 swarms, which occurred after the 2011 Tohoku-Oki earthquake, may have been triggered by a
57 reduction in fault strength due to upward pore pressure migrations (Terakawa et al., 2013; Okada
58 et al., 2015; Yoshida et al., 2016a, 2019a). Many natural seismic swarm activities, including the
59 examples above, have similar characteristics to fluid-injection-induced seismicity, such as the
60 migration behavior of the earthquake hypocenters. This similarity supports the hypothesis that
61 the swarm generation mechanism is essentially identical to fluid-injection-induced seismicity
62 (e.g., Cox, 2016).

63 Not only earthquake swarms but also foreshock-mainshock-aftershock sequences may be
64 closely-related to fluid behavior in the Earth. Sibson (1992) proposes a model in which the pore
65 pressure cycle controls the earthquake cycle due to over-pressurized fluids that rise from the
66 deeper portion of the fault (i.e., the fault-valve model). In this model, fault ruptures create
67 transient fracture permeability within the fault zone, acting as valves that promote the upward
68 discharge of fluids from deeper portions of the crust. This model is supported by various
69 geological and geophysical observations (Sibson, 2020). Hasegawa et al. (2005) propose a model
70 of the deformation process in a subduction zone based on various geophysical observations,
71 including seismic tomography results, in NE Japan. In this model, fluids expelled from the
72 subducting slab migrate upward, reaches the crust, and causes anelastic deformation of the crust,
73 including earthquakes.

74 Migration behavior of at hypocenters can be occasionally observed for fluid-injection-
75 induced seismicity and natural earthquake swarms (e.g., Shapiro et al., 1997; Yukutake et al.,
76 2011; Yoshida & Hasegawa, 2018a,b). There are two models that explain earthquake migration:
77 pore pressure migration and aseismic slip propagation. In the first mechanism, the migration of
78 hypocenters is presumed to reflect the migration of fluids (e.g., Shapiro et al., 1997; Talwani et
79 al., 2007). In the second mechanism, hypocenter migration is presumed to be a result of aseismic
80 slip propagation (e.g., Lohman & McGuire, 2007; Roland & McGuire, 2009). Both mechanisms
81 are likely responsible for the observed hypocenter migration behaviors, where the two
82 mechanisms can occasionally coexist (Waite & Smith, 2002; Ross et al., 2017; Yoshida &
83 Hasegawa, 2018; Barros et al., 2020). The space-time distributions of earthquake hypocenters
84 can be estimated more precisely than other seismological parameters, such as the fault slip and
85 seismic velocity. We can extract information on pore pressure migration and aseismic slip

86 propagation, which is crucial to understand the earthquake generation, by examining precisely-
 87 relocated hypocenters.

88 On Kyushu Island in Southern Japan, the volcanic front formed due to the subduction of
 89 the Philippine Sea Plate. Several of the most active volcanoes in Japan are distributed along this
 90 volcanic front (e.g., Sakurajima volcano and Aso volcano). Kagoshima Bay is located on this
 91 volcanic front, where a low gravity anomaly extends from north to south. On July 11, 2017, an
 92 M_{JMA} 5.3 strike-slip earthquake occurred at a depth of approximately 10 km in Kagoshima Bay
 93 (Fig. 1). Seismicity had been activated since December 2016 (Fig. 1(c)) near the mainshock
 94 hypocenter. For this foreshock activity, 1,843 events were located and listed in the Japan
 95 Meteorological Agency (JMA) unified catalogue. Seismicity had been increasingly active since
 96 the occurrence of the mainshock, i.e., 12,595 events were recorded in the JMA catalogue. Focal
 97 mechanisms of the earthquakes in this region, estimated by the JMA, show a strike-slip type with
 98 a NW-SE P-axis (Fig. 1(b)). Nanjo et al. (2018) suggest that fluid movement caused the
 99 earthquake sequence in Kagoshima Bay based on the spatiotemporal variation in the b-value and
 100 the migration behavior of the hypocenters.
 101



102
 103

104 *Figure 1. (a) A map showing southern Kyushu. Inverted triangles indicate the seismic stations.*
 105 *We used picked arrival time data obtained at stations in both blue and green. We analyzed*

106 *waveform data obtained at stations in green. The black square shows the target area of this*
107 *study. (b) Hypocenter distribution of earthquakes that occurred in Kagoshima Bay from January*
108 *1, 2010, to April 8, 2018, and their focal mechanisms. Hypocenters and focal mechanisms were*
109 *taken from the JMA unified catalog. The red square is defined as "the area around the*
110 *mainshock hypocenter" in this study. The numbers at the tops of the focal mechanisms indicate*
111 *the JMA magnitude of each earthquake. (c) M-T diagram and cumulative number of $M_{\text{JMA}} \geq$*
112 *1.0 earthquakes that occurred in the area surrounding the mainshock hypocenter (i.e., the red*
113 *square in Fig. 1(b)) prior to the mainshock. The vertical red line denotes the mainshock.*
114

115 In this study, we examine, in detail, the physical process behind the $M_{\text{JMA}} 5.3$ Kagoshima
116 Bay earthquake sequence in Kyushu, southern Japan. First, we precisely determine the
117 hypocenters and focal mechanisms of this earthquake sequence, as well as delineating the fault
118 structure. We also estimate the source size of the mainshock and examine its relationship with
119 the foreshocks and aftershocks to obtain a comprehensive view of this foreshock-mainshock-
120 aftershock sequence. We then examine the spatiotemporal characteristics of the intensive
121 foreshock and aftershock activity to extract information on the aseismic phenomena behind this
122 earthquake sequence. Finally, by integrating the obtained observations, we propose a model that
123 can explain the occurrence and characteristics of the foreshock-mainshock-aftershock sequence
124 associated with the 2017 $M5.3$ Kagoshima Bay earthquake.
125

126 2. Methods

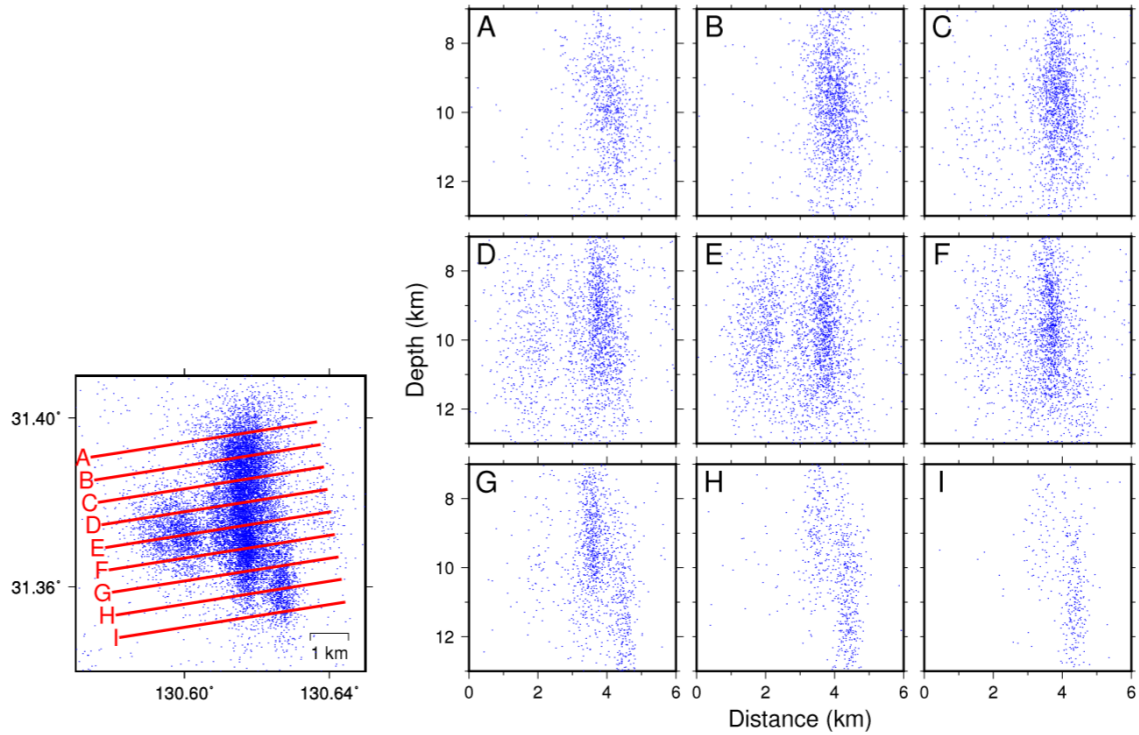
127 2.1. Hypocenter relocations

128 We relocated 18,390 events listed in the JMA unified catalogue in the southern Kagoshima
129 Bay region for the period from January 1, 2010, to April 8, 2018, using the Double-Difference
130 method (Waldhauser & Ellsworth, 2000). This relative relocation method minimizes the
131 residuals between the observed and theoretical travel time differences for adjacent earthquake
132 pairs at each station. We applied the Double-Difference method to the differential arrival time
133 data, which were precisely estimated from the waveform cross-correlation, and those listed in the
134 JMA unified catalog. The procedure is essentially identical to that reported in Yoshida and
135 Hasegawa (2018a,b), which is briefly described as follows.

136 First, we obtained precise differential arrival time data using waveform cross-correlations.
137 We used the waveform data observed at 20 permanent seismic stations that surround the focal
138 area (Fig. 1(a); green stations). At each station, the ground velocity is measured by three-
139 component short-period seismometers (natural period of 1s) and recorded at a 100 Hz sampling
140 rate. We applied a 5–12 Hz Butterworth filter to the waveforms of each target event obtained at
141 each seismic station. We used 2.8 s and 4.3 s time windows for the P- and S-waves, respectively,
142 beginning 0.3 s before the arrival times. Here, arrival times in the JMA unified catalogue were
143 used when listed. Otherwise, arrival times were estimated based on the 1-D velocity model, i.e.,
144 JMA2001 (Ueno et al., 2002), and the hypocenters and origin times listed in the JMA unified
145 catalogue. We calculated waveform cross-correlations of the event pairs, whose hypocenters
146 were located within 3 km of each other, and obtained the differential arrival times when the
147 cross-correlation coefficients were greater than 0.8. As a result, we acquired 23,077,393 P-wave
148 differential arrival time data and 37,128,628 S-wave data. We also derived the differential arrival
149 data from the arrival time data listed in the JMA unified catalog: 411,421 for P-wave and
150 467,687 for S-wave. For the mainshock, only data derived from the JMA unified catalog were
151 used due to its long source duration.

152 Second, we applied the hypo-DD algorithm (Waldhauser, 2001) to the differential arrival
153 time data. We used a spherical shell two-layer model (Aki, 1965) for hypocenter relocation. In
154 this model, seismic velocities vary in each layer in proportion to the power of the distance from
155 the center of the Earth (Fig. S1). The medium parameters were determined for consistency with
156 seismic tomography results of the Kyushu region (Saiga et al., 2010). We used the hypocenters
157 listed in the JMA unified catalogue for the initial locations for the relocation. Figure 2 shows the
158 distribution of these initial hypocenters. Differential arrival time data were weighted in
159 proportion to the square root of a cross-correlation coefficient. Hypocenters were updated during
160 50 iterations of the relocation procedure. In the first 10 iterations, we gave more weight to the
161 catalogue data to constrain the relative locations with a large scale. In the latter 40 iterations,
162 more weight was given to the data derived by the cross correlations to delineate shorter scale
163 features.

164



165
166
167
168
169
170
171
172

Figure 2. The distribution of the initial hypocenters listed in the JMA unified catalog. Blue dots indicate the locations of the hypocenters. The left figure is a map view while the right nine figures are the cross-sectional views along vertical sections indicated by the red lines from A to I in the left figure.

173

174 **2.2. Estimation of focal mechanisms**

175 We estimated the focal mechanisms based on the amplitude ratios of the waveforms using
 176 the method of Yoshida et al. (2019b) after Dahm (1996). We used six focal mechanisms
 177 determined by the JMA (Fig. 1(b)) for reference to the correct path- and site-effects on the
 178 waveform. We attempted to determine the focal mechanisms of 161 earthquakes with $M_{JMA} \geq 2$.
 179 We used displacement waveforms obtained by integrating the velocity waveform records over
 180 time at the 20 stations (green triangles in Fig. 1(a)) surrounding the hypocenters. The vertical
 181 component was used for the analysis of the P-wave while radial and transverse components were
 182 used for that of the S-wave. We applied a 2–5 Hz band-pass filter to the waveforms, cutting them
 183 out with time windows of 2.8 s for P-waves and 4.3 s for S-waves beginning 0.3 s before the
 184 arrival times.

185 We used waveform cross-correlations to measure the amplitude ratios between a target
 186 event and reference event. The amplitude ratios were obtained for the pairs when the absolute
 187 value of the correlation coefficient was higher than 0.75. We used principal component analysis
 188 (PCA) to measure the amplitude ratios.

189 We only estimated the mechanism solution when the amplitude ratios were obtained for
 190 more than 20 channels. We eliminated results for V.R. (Variance Reduction) less than 80 as
 191 follows:

$$V. R. = \left(1 - \frac{\sum_{k=1}^n (d_k - s_k)^2}{\sum_{k=1}^n d_k^2} \right) \cdot 100, \quad \#(1)$$

192

193 where d_k and s_k are the observed and calculated displacement amplitude ratios, respectively, at
 194 channel k .

195

196 **2.3. Estimation of mainshock source size**

197 We estimated the source size of the mainshock based on the circular-crack source model
 198 (e.g., Sato & Hirasawa, 1973; Madariaga, 1976). In these source models, the source radius is
 199 related to the S-wave corner frequency, f_c , as follows:

$$r = \frac{k\beta}{f_c}, \quad \#(2)$$

200 where r is the source radius, k is a constant, and β is the S-wave velocity near the source.
 201 Assuming a rupture velocity of 0.9β , k is 0.44 in the model of Sato and Hirasawa (1973) and
 202 0.32 in the model of Madariaga (1976) for P-waves. As the estimated source size depends on the
 203 adopted source model, we computed the fault size using both models. We assumed $\beta = 3.4$ km/s.

204 We used the spectral ratio method (e.g., Imanishi & Ellsworth, 2006) to estimate the
 205 corner frequency of the mainshock. In this method, propagation- and site-effects on the seismic
 206 wave are empirically removed using the waveforms of an adjacent small earthquake (EGF
 207 event). Assuming that the source spectrum, i.e., $S_j(f)$, follows the ω^2 model (Aki, 1967; Brune,
 208 1970), the theoretical ratio between the velocity spectra of the mainshock, $v_i(f)$, and the EGF
 209 event, $v_i^{egf}(f)$, at station- i is as follows:

$$SSR_{ij}(f) = \frac{v_i(f)}{v_i^{egf}(f)} = \frac{M_0}{M_0^{egf}} \frac{R_{\theta\phi i}}{R_{\theta\phi i}^{egf}} \frac{1 + \left(\frac{f}{f_c^{egf}}\right)^2}{1 + \left(\frac{f}{f_c}\right)^2} \quad \#(3)$$

210 ,
 211 where M_0 and M_0^{egf} are the seismic moments of the target earthquake and EGF event,
 212 respectively, $R_{\theta\phi ij}$ and $R_{\theta\phi i}^{egf}$ are their radiation patterns at station i , respectively, and f_c^{egf} is the
 213 corner frequency of the EGF event. Based on Eq. (3), we can estimate f_c from the shape of the
 214 spectral ratios.

215 We calculated spectral ratios using observed P-wave velocity waveforms at the 20 stations
 216 surrounding the source area (green inverted triangles in Fig. 1(b)). The EGF events were
 217 earthquakes with $M \geq 2$, whose distance from the mainshock was < 1.0 km based on the
 218 relocated hypocenters. The procedure was performed as follows with reference to Yoshida et al.
 219 (2017):

220 (1) For the target mainshock and EGF events, waveforms of the three components were
 221 cut out for a 2.0 s time window starting 0.3 s before the arrival time of the P-wave at each
 222 station. The multitaper method (Thomson, 1982; Prieto et al., 2009) was applied to
 223 calculate the spectra.

224
 225 (2) For the channels where the EGF observation spectrum always satisfied $S/N > 2$ in the
 226 frequency range of 0.5–30.0 Hz, the spectral ratio was calculated between the mainshock
 227 and EGF event. Here, we used waveforms up to 0.3 s before the arrival time of the P-
 228 waves for the noise window.

229
 230 (3) We calculated the geometric mean of the spectral ratios $GSR(f)$ of all the channels at
 231 each frequency point for the EGF events, which satisfied the above criterion at 5 or more
 232 stations as follows:

$$GSR(f) = \prod_{i=1}^N (SR_i(f))^{\frac{1}{N}}, \#(4)$$

233 where $SR_i(f)$ is the observed spectral ratios obtained at station i and N is the number of
 234 stations.

235
 236 (4) Using the grid search, the corner frequencies of the mainshock, f_c , and EGF event,
 237 f_c^{egf} , were determined by minimizing the following evaluation function, J :

$$J = \sum_{k=1}^{n_{freq}} \left| \log(GSR(f_k)) - A \log(NSR(f_k; f_c, f_c^{egf})) \right| \#(5)$$

238
 239 where $NSR(f; f_c, f_c^{egf}) = \frac{1+(f/f_c^{egf})^2}{1+(f/f_c)^2}$, n_{freq} is the number of frequency points and f_k is
 240 frequency point at 0.5 Hz intervals from 0.5 to 30 Hz. The grid search was performed for
 241 f_c and f_c^{egf} while assuming a range from 0.1 to 100 Hz at 0.1-Hz-steps. The amplitude
 242 ratio, A , was estimated using the least squares method at each grid-search step.

243
 244 We applied the spectral ratio method to 33 EGF candidates. As a result, we obtained
 245 spectral ratios from 21 EGF events, which satisfy our criteria for the S/N ratio and data number.
 246 Figure S2 shows the spectral ratios from the 21 EGF events.

247

248 **2.4. Detection of aseismic process from seismicity**

249 Previous studies have reported that seismic activity caused by external forces, such as fluid
 250 movements or aseismic slips, has different characteristics from the mainshock-aftershock
 251 sequence type (e.g., Hainzl & Ogata, 2005; Roland & McGuire, 2009; Kumazawa & Ogata,
 252 2013; Yoshida & Hasegawa, 2018b). This suggests that investigating seismicity may provide
 253 clues to the aseismic processes behind the occurrences of earthquakes.

254 The Epidemic Type Aftershock Sequence (ETAS) model (Ogata, 1988), based on the
 255 superposition of the modified Omori law (Utsu, 1961), can appropriately explain mainshock-
 256 aftershock seismicity. The ETAS model assumes that the seismicity rate is a summation of the
 257 background rate of independent events, λ_0 , and aftershocks triggered by each event, $\lambda_i(t)$, as
 258 follows:

$$\lambda(t) = \lambda_0 + \sum_{i:t_i < t} \lambda_i(t) \#(6)$$

259 .
 260 Each earthquake can trigger its own aftershock sequence following the modified Omori Law
 261 (Utsu et al., 1995) as follows:

$$\Lambda_i(t) = \frac{K_0}{(c+t-t_i)^p} e^{\alpha(M_i - M_{\min})} \#(7)$$

262 ,
 263 where t_i is the occurrence time; M_i is the magnitude of each event, $-i$, that occurred prior to
 264 time t ; M_{\min} is the magnitude of completeness of the earthquake catalogue; K_0 , c , and p are
 265 constants; and t is the elapsed time since the main event.

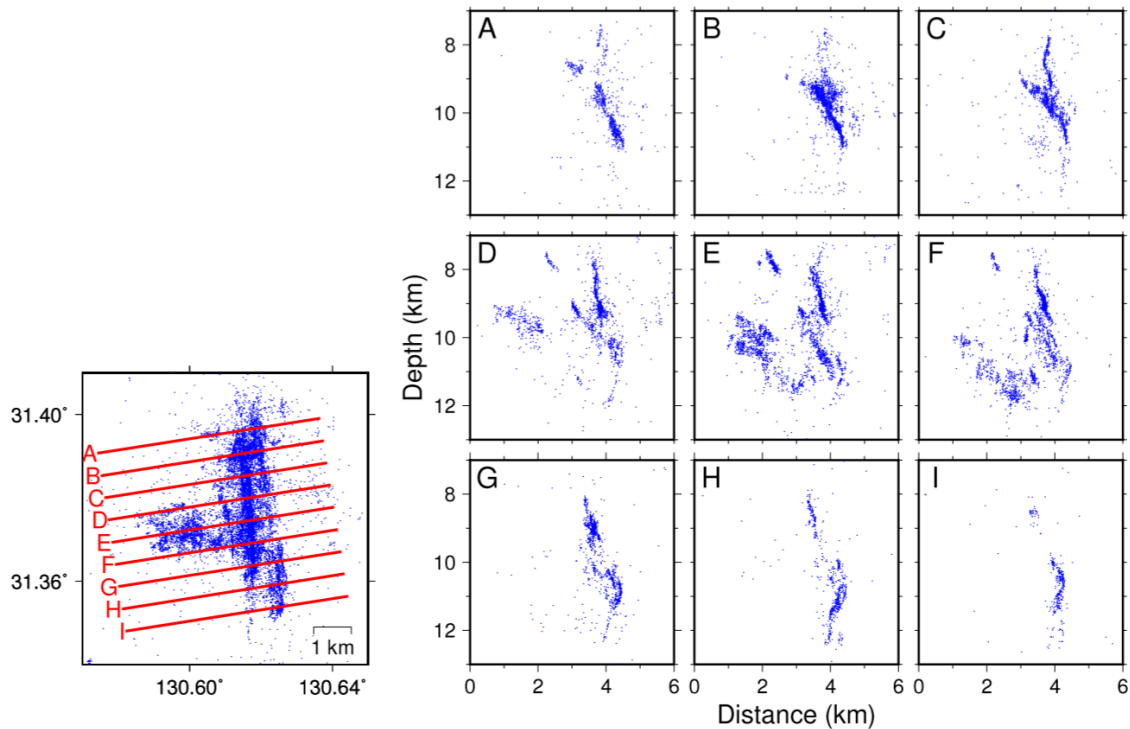
266 We applied the ETAS model to the seismicity observed after the mainshock in Kagoshima
 267 Bay and investigated the difference between the simulated and observed seismicity. We found
 268 that the foreshock activity cannot be explained by the ETAS model, which is likely because the
 269 aseismic process mainly controlled the foreshock activity. We used the timings and magnitudes
 270 of the earthquakes listed in the JMA catalogue. The lower limit of magnitude, M_C , was set to 1.0.
 271 Figure S3 shows the magnitude-frequency distribution. The distribution appears to follow the
 272 Gutenberg-Richter law (Gutenberg & Richter, 1944) when $M_{\text{JMA}} \geq 1.0$. The SASEis2006
 273 algorithm by Ogata (2006) was used for model parameter estimation and residual analysis in the
 274 ETAS model.
 275
 276
 277
 278

279 **3. Results**280 **3.1. Fault structure and seismic gap**

281 We obtained the relocated hypocenters of 18,211 events and focal mechanisms of 61
 282 events. Nearly all the events in the Kagoshima-Bay earthquake sequence can be precisely
 283 relocated by the Double-Difference algorithm. Location data for 179 earthquakes were removed
 284 because their hypocenters were located above the ground surface or they included outliers in the
 285 differential arrival time data.

286 Figure 3 shows the distribution of relocated hypocenters. Most hypocenters were located
 287 within ~5 km from the mainshock hypocenter and distributed along several planes. This
 288 characteristic is in contrast to the distribution of the initial hypocenters (Fig. 2), which were
 289 scattered three-dimensionally similar to a cloud. This drastic change in the hypocenter
 290 distribution derives from the improvements to the relative locations of the hypocenters in this
 291 study due to numerous and precise differential arrival time data. Such dramatic improvements to
 292 the relative hypocenters for the shallow earthquakes, from a cloud-like distribution to planar
 293 structures, were also reported in previous studies from Japan based on a similar method (e.g.,
 294 Yoshida & Hasegawa, 2018a,b). The cloud-like distribution of the initial hypocenters actually
 295 reflects the determination error of hypocenter locations in the JMA unified catalog due to errors
 296 in manual picking.

297



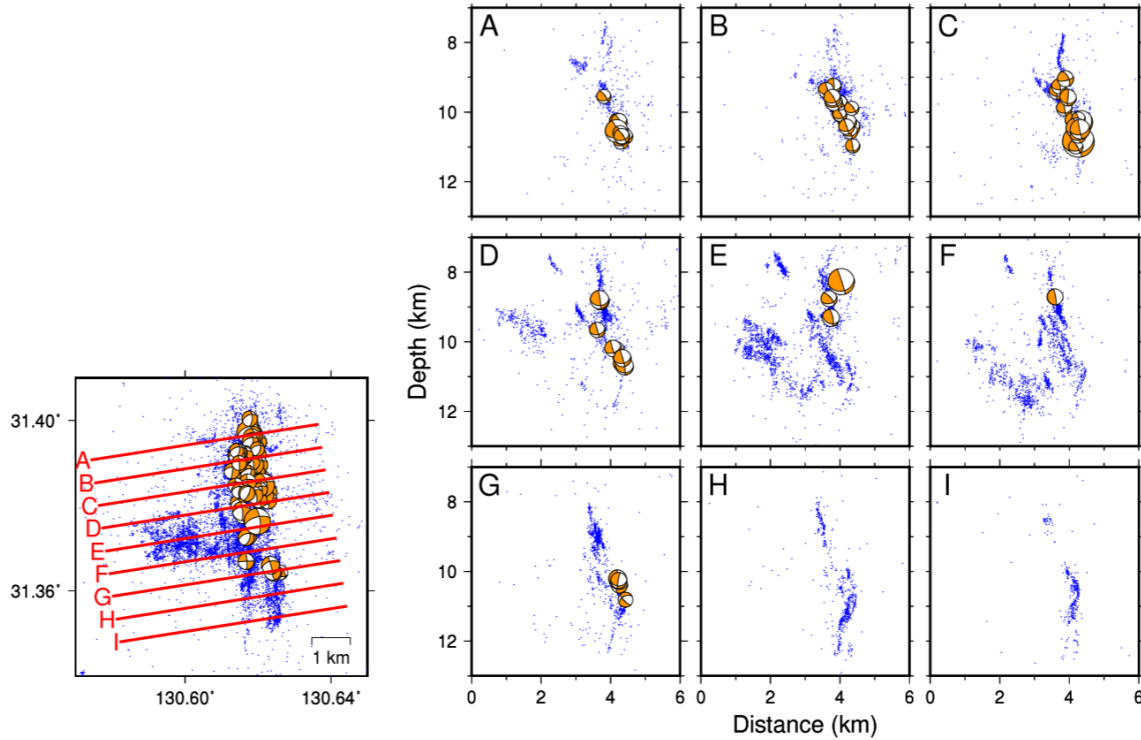
298

299 *Figure 3. Distribution of the relocated hypocenters based on the DD method. Blue dots indicate*
 300 *the locations of the hypocenters. The left panel is a map view while the right nine figures (A–I)*
 301 *are the cross-sectional views along the vertical sections indicated by the red lines from A to I in*
 302 *the left figure.*

303

304

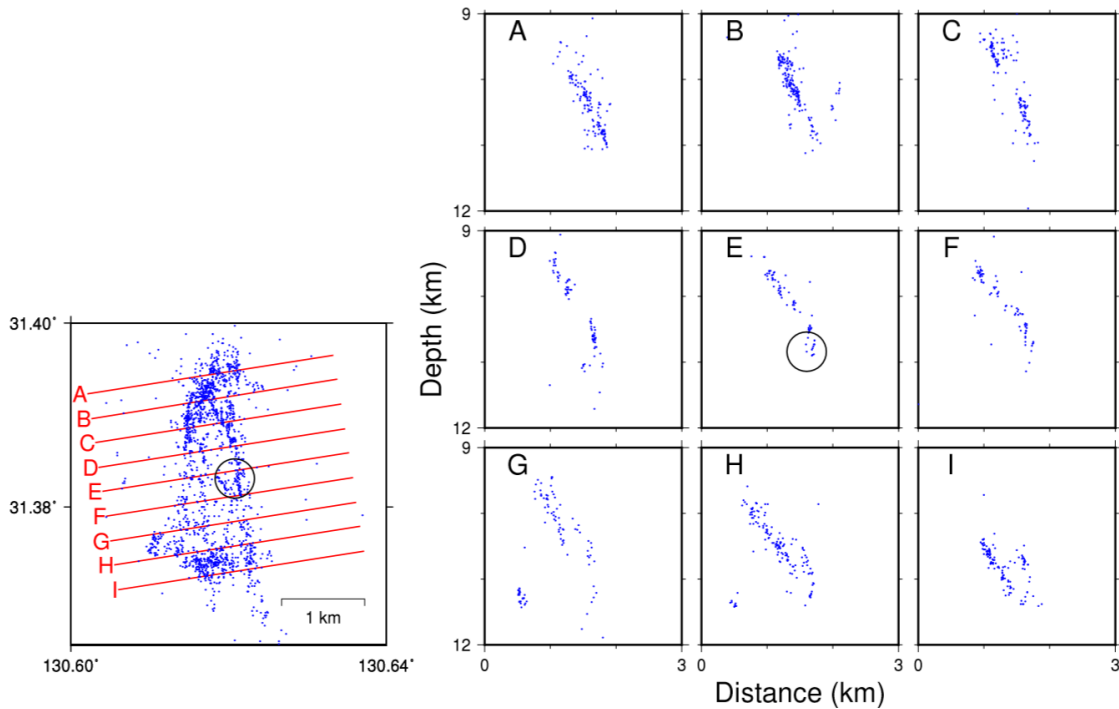
305 Figure 4 shows the spatial distribution of the focal mechanisms. As the reference focal
 306 mechanisms are located in the northern part of the source region (Fig. 1(b)), newly-estimated
 307 focal mechanisms are mainly located in the northern part. We can observe that the nodal planes
 308 for most focal mechanisms are parallel to the planar structures of the hypocenters, suggesting
 309 that these individual small earthquakes occurred on several macroscopic planes.
 310



311
 312
 313 *Figure 4. The estimated focal mechanisms plotted on the hypocenter distribution. The left figure*
 314 *is a map view and the right nine figures (A–I) are cross-sectional views along vertical sections*
 315 *indicated by the red lines from A to I in the left figure.*

316
 317 Based on Figs. 3 and 4, the fault structures of the 2017 Kagoshima Bay earthquake
 318 sequence appear to be quite complex, consisting of several subparallel planes. However, the
 319 distribution of hypocenters was relatively simple before the mainshock. Figure 5 shows the
 320 spatial distribution of hypocenters with respect to the foreshock activity. Most hypocenters are
 321 neatly distributed on one plane with the strike parallel to ones of the nodal planes of the focal
 322 mechanisms in the mainshock and individual small earthquakes, suggesting that most foreshocks
 323 and the mainshock occurred on this plane.

324



325
326

327 *Figure 5. The hypocenter distribution of the foreshock activity. The left panel is a map view. The*
 328 *right nine figures (A–I) show the hypocenters projected onto the vertical sections on the red lines*
 329 *from A to I in the left panel. The large black circle indicates the hypocenter location of the*
 330 *mainshock.*

331

332 The hypocenters of the foreshock activity are not uniformly distributed on this plane, but
 333 are distributed in a doughnut shape to avoid the center of the plane forming a seismic gap. The
 334 hypocenter of the mainshock is located at an edge of this seismic gap. Figure S4 compares the
 335 hypocenters of the foreshocks to those of the aftershocks. Although the aftershocks appear to
 336 occur inside the seismic gap based on the map-view, they actually occurred in a portion
 337 shallower than the foreshocks. Aftershocks also avoided any occurrences in the seismic gap of
 338 the foreshock activity.

339 This doughnut-like pattern in the foreshocks is similar to what is known as the “Mogi
 340 doughnut” (Mogi, 1969). Aftershocks have also been reported to have avoided occurrences along
 341 the segment with the rupture of the mainshock (e.g., Mendoza & Hartzell, 1988; Das & Henry,
 342 2003; Woessner et al., 2006; Asano et al., 2011; Ebel & Chambers, 2016; Yoshida et al., 2016b;
 343 Ross et al., 2017 & 2018; Wetzler et al., 2018) likely because the mainshock released the shear
 344 stress at this point. Therefore, the mainshock rupture of the Kagoshima Bay earthquake sequence
 345 may have mainly occurred in this seismic gap. The median value of the estimated corner
 346 frequencies of the mainshock was 2.1 Hz (Fig. S2). The first and third quartiles were 1.9 and 2.5
 347 Hz, respectively. Based on the median corner frequency, the source radius of the mainshock is
 348 710 m according to the model proposed in Sato and Hirasawa (1973) and 520m using the model
 349 proposed in Madariaga (1976). In Fig. S5, the size of the seismic gap was compared with the
 350 estimated fault size of the mainshock. The fault size of the mainshock falls within the seismic
 351 gap. This is consistent with our estimation that the mainshock rupture occurred in the seismic
 352 gap of the foreshock and aftershock activities. A similar spatial separation in the rupture area of

353 the mainshock with the foreshock and aftershock activities was also reported for a recent M5.2
 354 intraplate earthquake in Akita, NE Japan (Yoshida et al., 2020).

355

356 **3.2. Foreshocks and aftershock migration behaviors**

357 Figure 6 shows the occurrence timings of the foreshock activity based on a color scale.

358 Foreshocks were mainly located in the northern part at the beginning, but gradually moved

359 toward the southern part. Figure 7a, 7b, and 7c compare the occurrence timing of each

360 earthquake with the longitude, latitude, and depth, respectively, which illustrate the migration

361 behavior. In the longitudinal direction (Fig. 7a), the hypocenters expanded nearly symmetrically

362 in the first 230 days of foreshock activity, concentrating on the east side, i.e., the location of the

363 mainshock hypocenter during the last ~70 days of activity. In the latitudinal direction (Fig. 7b),

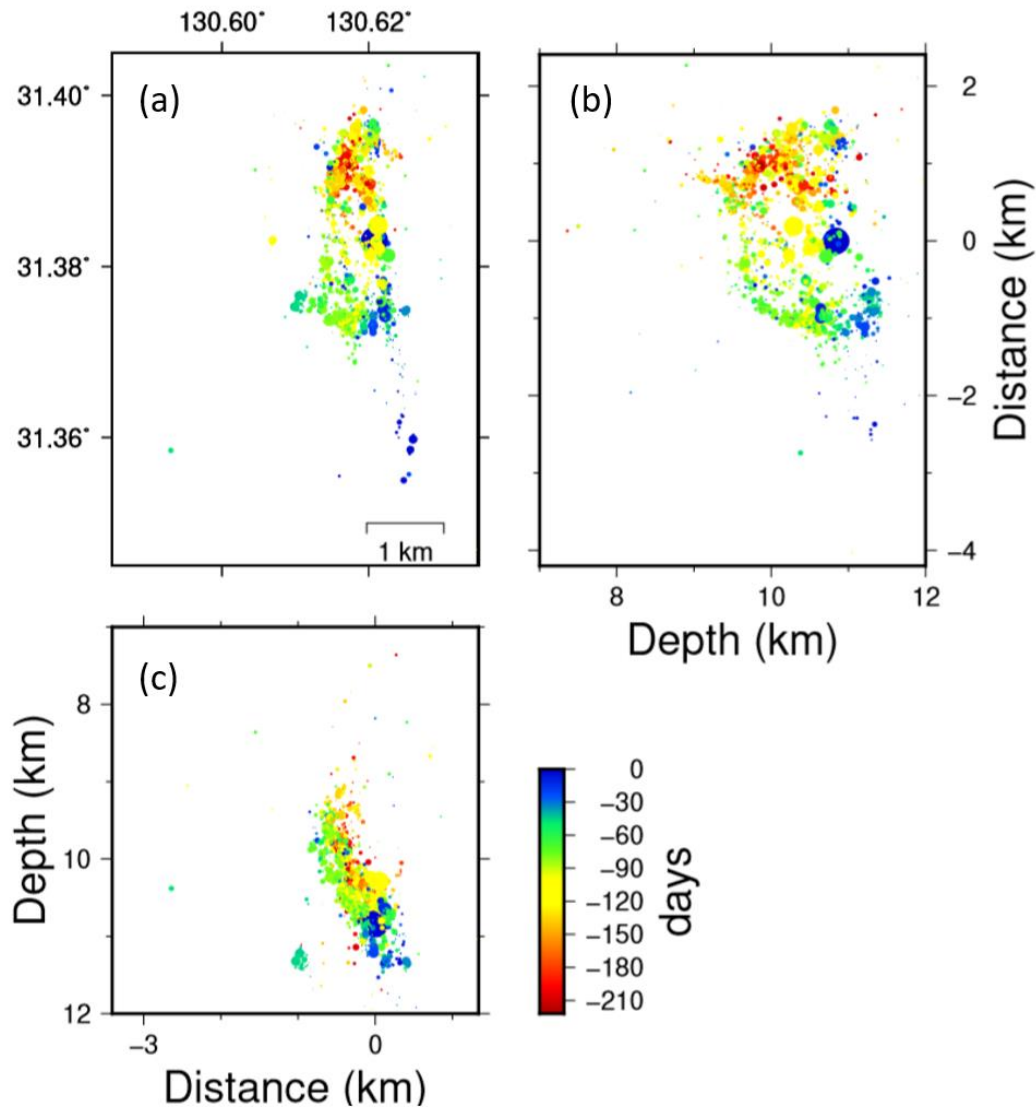
364 the hypocenters evidently migrated from the north to the south. In the depth direction (Fig. 7c),

365 the hypocenters migrated both in the shallow and deep directions, such that most earthquakes

366 occurred in the deeper part, i.e., the location of the mainshock hypocenter during the last ~70

367 days of activity.

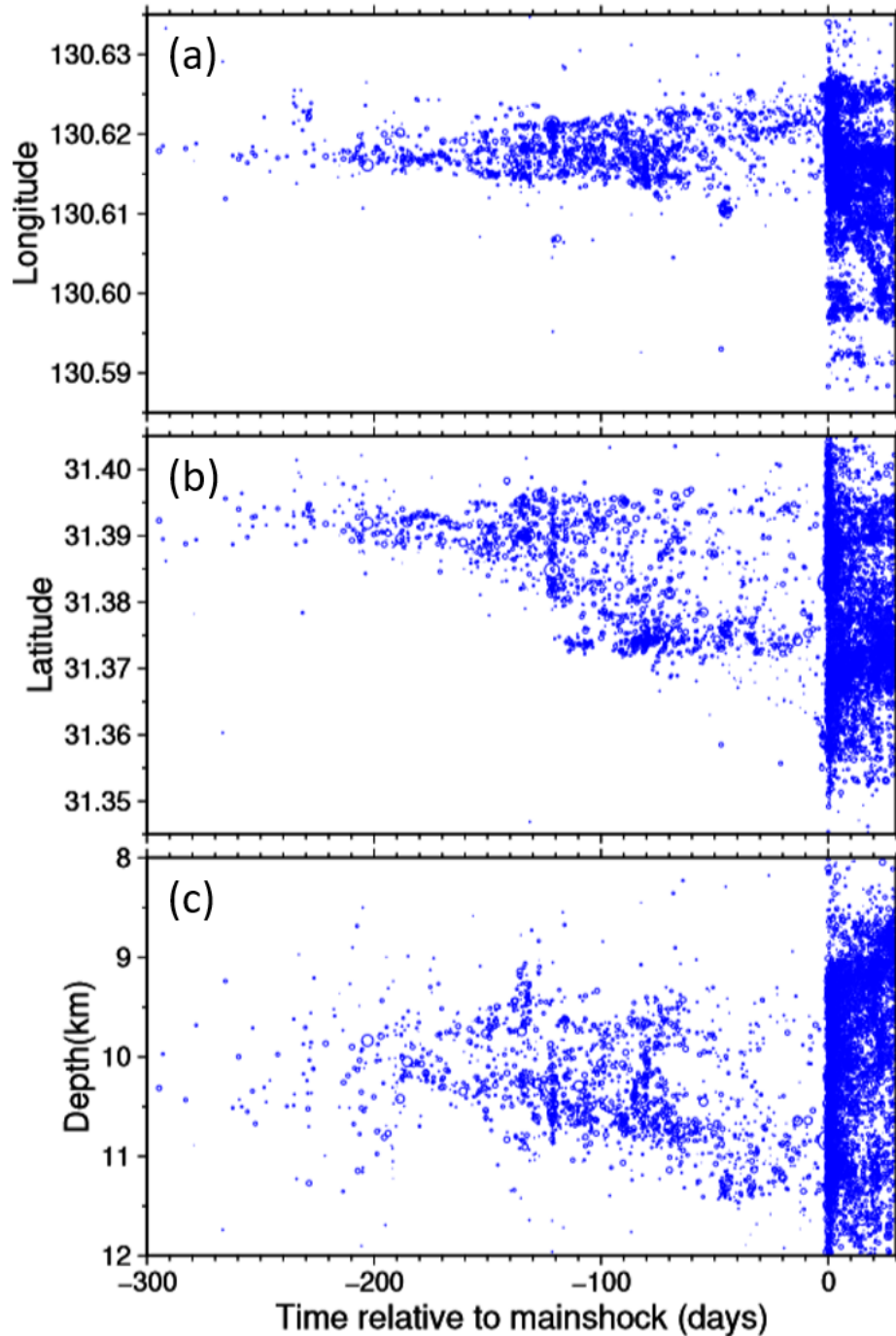
368



369

370
371
372
373
374
375
376
377
378

Figure 6. Spatiotemporal evolution of the hypocenters as a function of the foreshock activity. The hypocenters projected onto (a) the map view, (b) the north–south vertical cross-section, and (c) the east–west vertical cross-section, where the symbol sizes correspond to the JMA magnitudes. The hypocenters are colored according to the occurrence time measured relative to that of the mainshock, i.e., the mainshock as time 0, with negative days denoting hypocenters before the mainshock.



379

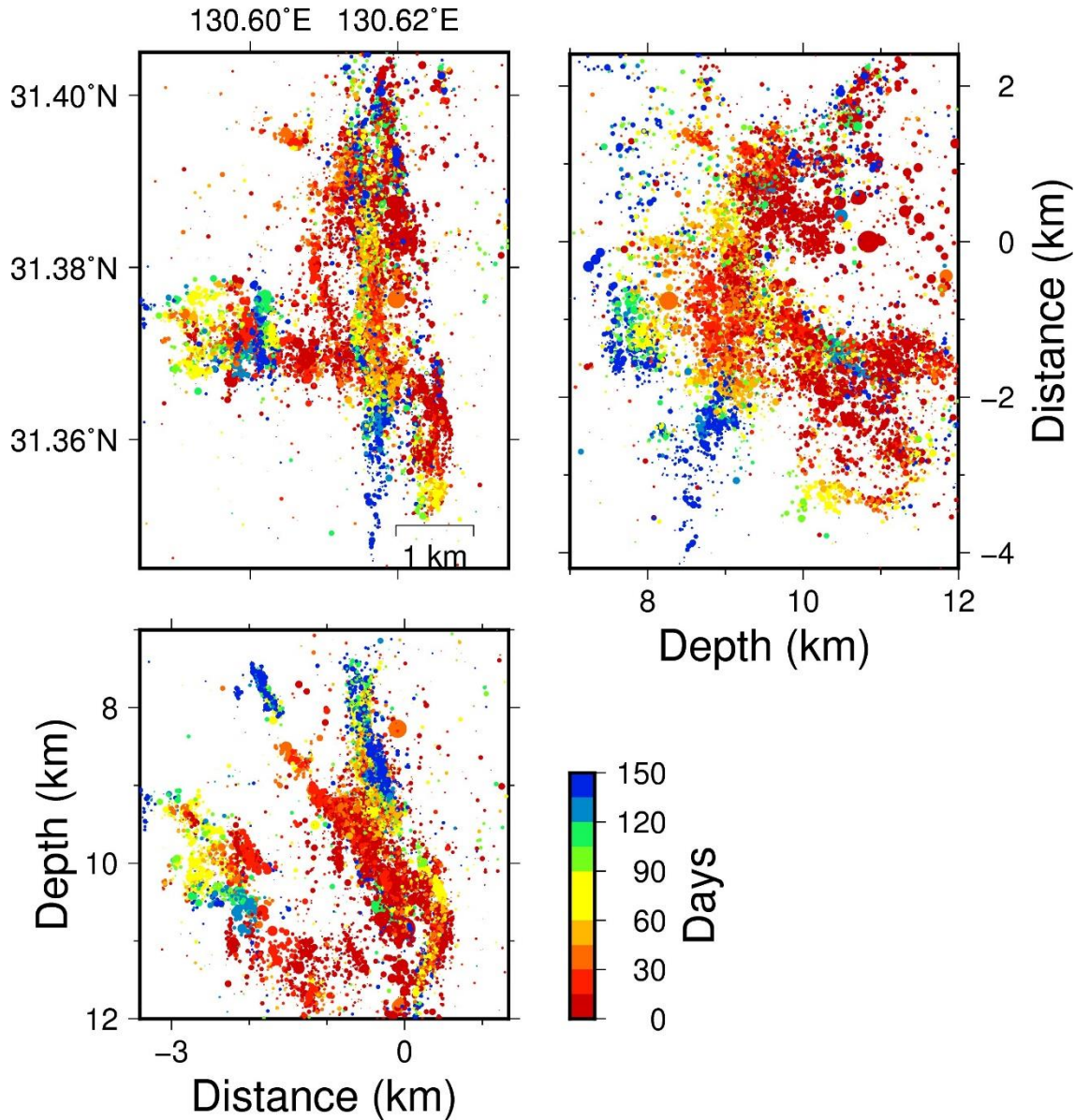
380

381 *Figure 7. Temporal evolution of hypocenters in the (a) latitude, (b) longitude, and (c) depth*
382 *directions. The circle size corresponds to the JMA magnitude.*

383

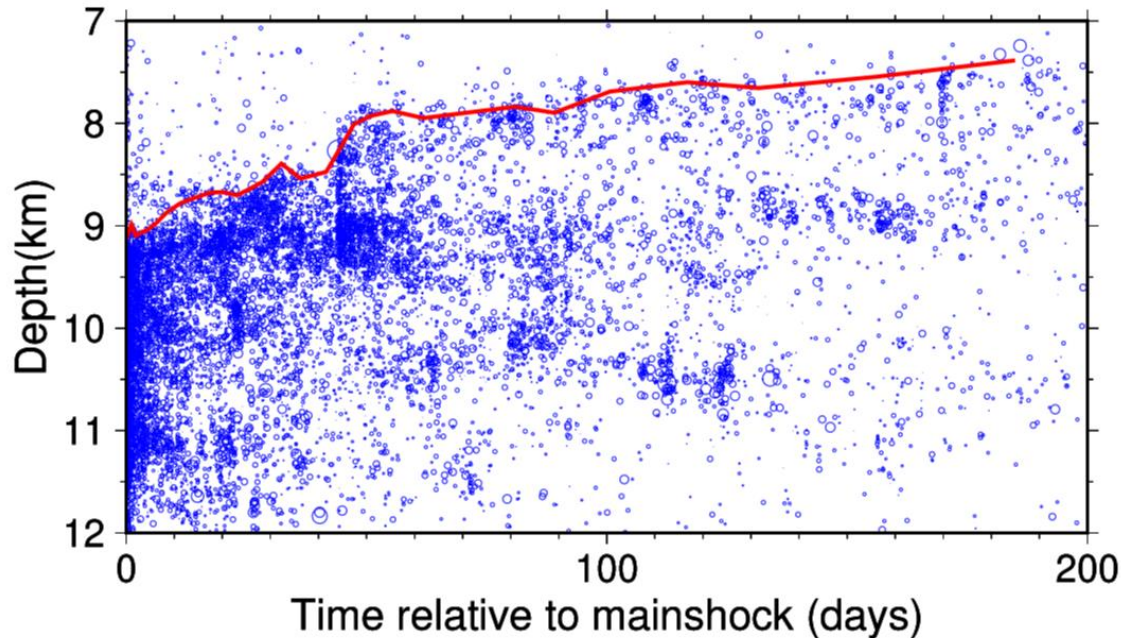
384 Figure 8 shows the distribution of aftershock hypocenters colored by the occurrence time
385 of each event. Figure 9 shows the temporal evolution of the aftershock hypocenters as a function
386 of the depth. Furthermore, Fig. S3 shows the temporal evolution of the aftershock hypocenters in
387 both the latitudinal and longitudinal directions. As the spatial distribution of the aftershocks is
388 complex, the spatiotemporal features of the aftershock activity are more difficult to examine than
389 that of the foreshock activity. Overall, the aftershock hypocenters moved upward with time as
390 shown in Fig. 9, which depicts the depths above which the shallowest 5% of the hypocenters are
391 located (D05), where each bin contains 400 events, as denoted by the red curve. Although
392 earthquakes occurred in a relatively deep region immediately after the mainshock, the upper limit
393 of the seismic depth (D05) gradually expanded in the shallow direction, i.e., the hypocenters
394 gradually moved to the shallower part with time after the mainshock.

395



396
397
398
399
400
401
402

Figure 8. Spatiotemporal evolution of the aftershock hypocenters. The hypocenters projected onto the (a) map view, (b) north–south vertical cross-section, and (c) east–west vertical cross-section, shown by circles with sizes corresponding to the JMA magnitude. The hypocenters have specific colors based on the occurrence time measured from that of the mainshock.



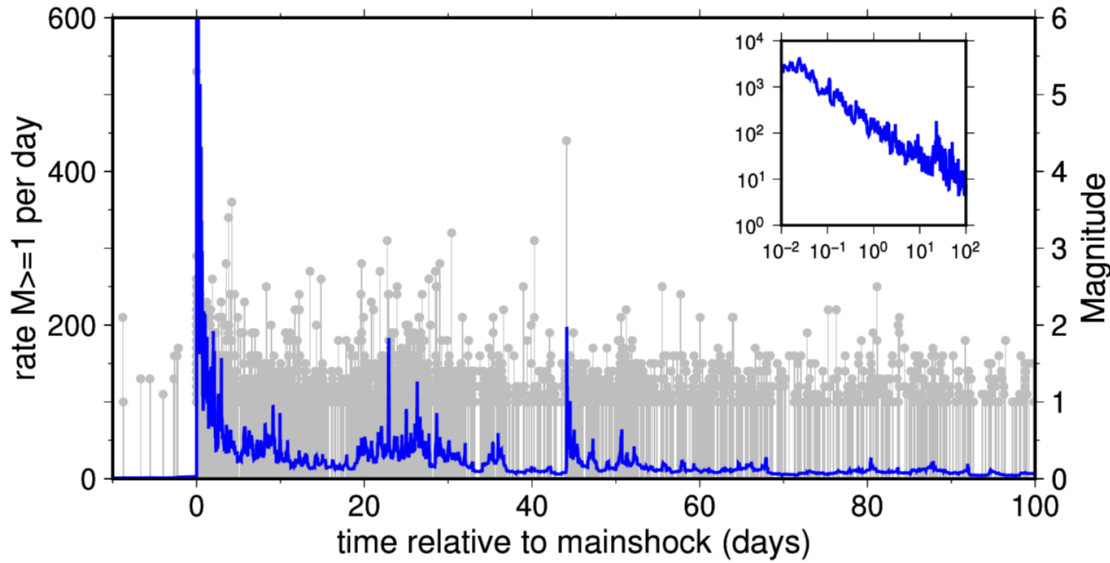
403
404
405
406
407
408
409
410

Figure 9. The temporal evolution of the aftershock hypocenters in the depth direction. Circle size corresponds to the JMA magnitude. The red line indicates the depth above which the shallowest 5% of the hypocenters are located (D05) at every bin with 400 events in order of occurrence time.

411
412
413
414
415
416
417
418
419
420
421
422
423

3.3. Seismicity deviation from Omori's law

We investigated the seismicity rate of the Kagoshima Bay earthquake sequence after the mainshock. Figure 10 shows the seismicity rate of the $M_{\text{JMA}} \geq 1.0$ events in the area around the mainshock hypocenter (red frame in Fig. 1(b)). The seismic rate was obtained by calculating the reciprocal of the time required to generate ten earthquakes arranged in chronological order. According to Fig. 10, the seismicity rate decreased by a power of the elapsed time immediately after the mainshock, as described by the modified Omori law. We observe that the seismicity rate abruptly increased ~ 44 days after the mainshock, which corresponds to the occurrence of the largest aftershock at $M_{\text{JMA}} 4.4$, suggesting an increase due to secondary aftershocks. Also, there a high-seismicity-rate period appears from approximately 20 to 40 days after the mainshock, during which the seismic activity is temporarily high despite no large aftershocks.



424
425

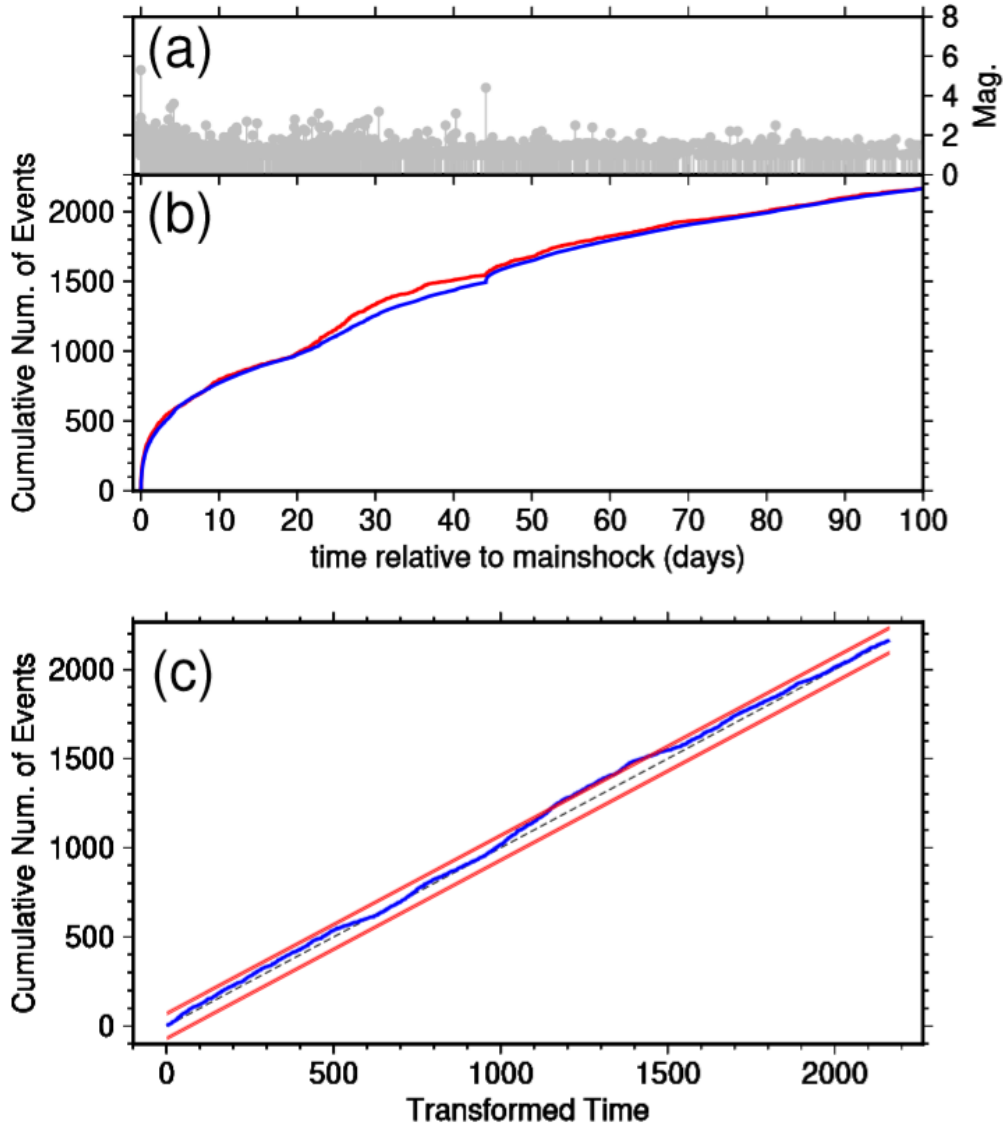
426 *Figure 10. Aftershock occurrence rate of the $M_{JMA} \geq 1.0$ events (blue) and the M-T diagram*
427 *(gray). Inset compares the aftershock occurrence rate with time on a log-log scale. The*
428 *occurrence rate was estimated by calculating the reciprocal of the time when 10 events occurred*
429 *with $M_{JMA} \geq 1.0$.*

430

431 As a result of the maximum likelihood estimation, the ETAS model parameters were
432 estimated as $K_0 = 45.479$, $c = 0.85120 \times 10^{-2}$, $p = 0.97934$, $\alpha = 1.6096$, and $\mu =$
433 0.18287×10^{-13} . According to Ogata (1992), the range of α -values is [0.35, 0.85] for swarm
434 seismicity and [1.2, 3.1] for non-swarm seismicity. For the seismic activity in Kagoshima Bay,
435 the estimated α value was within the latter range.

436

437 Figure 11 compares the cumulative number of earthquakes simulated from the estimated
438 model parameters with its observed counterpart. The number predicted based on the ETAS
439 model appears to sufficiently explain the overall observed trend. However, the simulated number
440 of earthquakes is apparently lower than the observed number for the period from 20 to 40 days
441 after the mainshock. To quantitatively examine the degree of discrepancy between the model and
442 observation, we performed a residual analysis using the transformed time, similar to Ogata
443 (1988). Figure 11c shows that the discrepancy between the model and observation began to
444 increase at the transformed time of approximately 1,000, which corresponds to approximately 20
445 days after the mainshock. This difference exceeded the 99% significance level assuming a
uniform distribution.



446
447

448 *Figure 11. (a) The M-T diagram. (b) Observed cumulative number of aftershocks with $M_{JMA} \geq$*
 449 *1.0 (red solid line) and predicted number based on the estimated ETAS parameters (blue solid*
 450 *line). Each represents the cumulative numbers from 0.1 day after the mainshock. (c) Results of*
 451 *the residual analysis, where the blue solid line shows the observed events with respect to the*
 452 *Transformed Time on the horizontal axis and cumulative number of observed $M_{JMA} \geq 1.0$*
 453 *earthquakes on the vertical axis. The black dotted line represents the Transformed Time when*
 454 *the assumed model can entirely explain the observation. The red solid lines indicate the two-*
 455 *sided 95 and 99% error bounds of the Kolmogorov- Smirnov statistic.*

456

457

458 The large discrepancy between the predicted and observed seismicity rates from 20 to 40
 459 days (~1,000–1,500 in Fig. 11(c)) after the mainshock can be understood as temporary increases
 460 in the background seismic activity, which was assumed to be constant over the entire period of
 461 this analysis. The transient increase in the background seismicity rate suggests that the

462 Kagoshima Bay earthquake sequence may have been affected by physical processes other than
463 interseismic interactions, especially during this period. During this period, the aftershock
464 hypocenters rapidly migrated upward (Fig. S7). On the other hand, most aftershocks can be
465 explained as general mainshock-aftershock seismic activity, likely suggesting that stress changes
466 caused by the mainshock resulted in numerous aftershocks.

467

468

4. Discussion

Our results show that: (1) foreshocks in the 2017 M5.3 Kagoshima Bay earthquake sequence occurred on a single plane steeply inclined to the east while aftershocks occurred on several more complex planar structures, (2) the foreshock hypocenters form a seismic gap, whose size is comparable to the source size of the mainshock, and (3) the foreshock and aftershock hypocenters exhibit clear migration behaviors. In this section, we attempt to integrate these observations and propose a simple model that can explain the occurrence of the foreshock-mainshock-aftershock sequence of the 2017 M5.3 Kagoshima Bay earthquake based on upward fluid movement, which is similar to the model proposed by Sibson (1992).

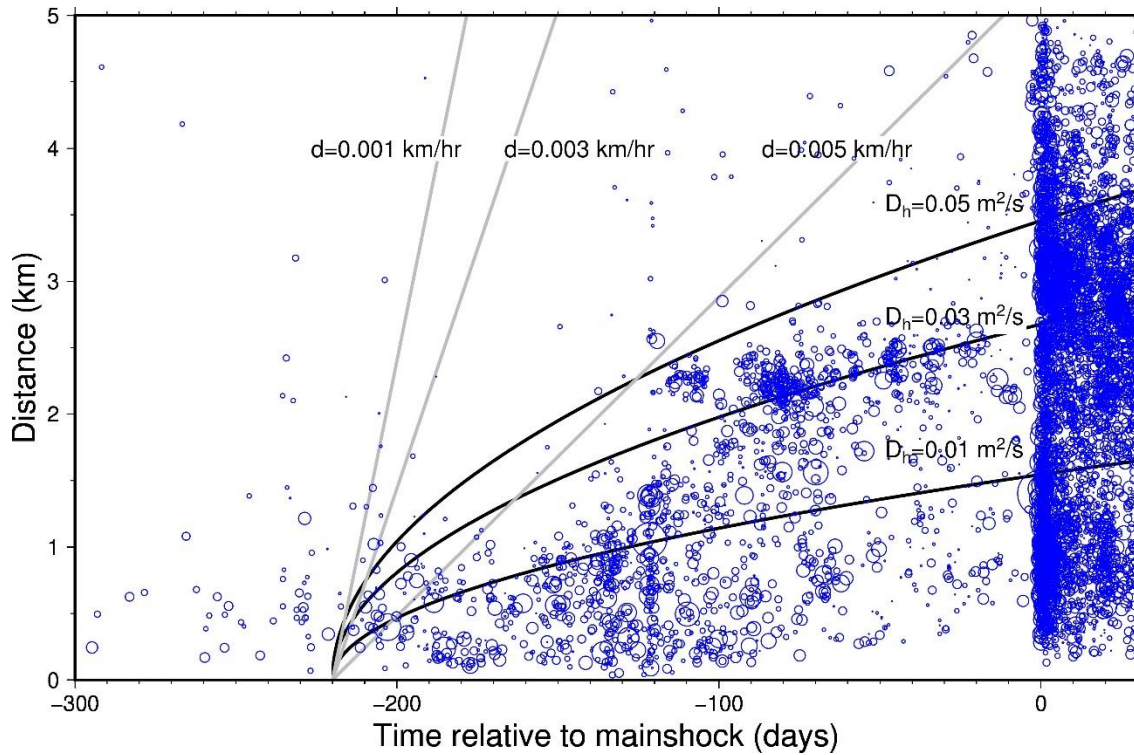
4.1. Migration of foreshock activity along a plane

Possible causes of hypocenter migration are aseismic processes, such as fluid movement (e.g., Talwani & Acree, 1985; Shapiro et al., 1997) and aseismic slip (e.g., Lohman & McGuire, 2007; Roland & McGuire, 2009). The observed migration behaviors suggest that such aseismic processes played important roles in the generation of the earthquake sequence in Kagoshima Bay.

Figure 12 compares the distances of the foreshock hypocenters from the first event with time. We also show, in Fig. 12, the expansion front of the pore pressure diffusion model reported in Shapiro et al. (1997), represented by the following formula with various diffusion coefficients D_h :

$$r = \sqrt{4\pi D_h t}, \#(9)$$

where r is the distance from the point pressure source and t is time. Here, we set the initiation time to 220 days before the mainshock because the seismicity rate significantly increased at this time (Fig. 1c). We also show the propagation fronts of the linearly-spreading model, which previous studies have occasionally assumed for aseismic slip propagation (e.g., Vidale & Shearer, 2006).



495
496

497 *Figure 12. The temporal evolution of the distances between the foreshock activity and the initial*
498 *hypocenter. Blue circles represent the hypocenters expressed by the size corresponding to the*
499 *JMA magnitudes. The black curves show the fluid diffusion models with $D_h = 0.01, 0.03,$ and*
500 *$0.05 \text{ m}^2/\text{s}$. Gray straight lines show the linear spreading model with migration speeds of*
501 *$d=0.001, 0.003,$ and 0.005 km/hr .*

502

503

504

505

506

507

508

509

510

511

512

513

514

515

516

517

518

519

520

We can observe that the pore pressure diffusion model yields a better fit to the observation than the linear spreading model when the hydraulic diffusion coefficient is approximately $0.05 \text{ m}^2/\text{s}$. Previous studies have estimated the hydraulic diffusion coefficients in the crust to range from $\sim 0.01\text{--}10 \text{ m}^2/\text{s}$ (e.g., Talwani et al., 2007; Shelly et al., 2016; Yoshida & Hasegawa, 2018a), which is similar to the foreshock migration speed of the M5.3 Kagoshima Bay earthquake sequence. If we assume the linear spreading model, the propagation velocity is approximately $0.001\text{--}0.005 \text{ km/h}$. Previous studies have obtained a range of migration speeds for aseismic slip propagations from $0.1\text{--}1.0 \text{ km/h}$ (e.g., Lohman & McGuire, 2007; Kato et al., 2016), which is significantly higher than the migration speed of the present foreshock activity. If we advance the initiation timing of propagation, the propagation speed becomes even slower. Thus, according to the migration speed and spatiotemporal pattern of foreshocks, the pore pressure diffusion model is more appropriate for explaining the overall migration of the foreshock hypocenters.

Recent observations of fluid-injection-induced seismicity and natural earthquake swarms, however, suggest that an increase in the pore pressure can also trigger aseismic slips (Cornet et al., 1997; Guglielmi et al., 2015; Yoshida & Hasegawa, 2018a; Barros et al., 2020). In the presence of fluids, there is a decrease in the effective normal stress and an increase in the critical nucleation size, such that the occurrence of aseismic slip may be a more likely phenomena (e.g.,

521 Scholz, 1998; Rubin & Ampuero, 2005). Both aseismic slips and fluid movements may have
522 contributed to the occurrence of foreshock activity.

523 Physical simulations indicate that interseismic creep penetrates seismogenic patches from
524 external stable-slip regions before the occurrence of unstable slip in the seismogenic patches
525 (Tse & Rice, 1986). Such an expansion of quasi-static slip prior to the mainshock may explain
526 the currently observed migration behaviors in the foreshock activity (e.g., Dodge et al., 1996;
527 Yabe & Ide, 2018). The source size of the mainshock rupture, however, is smaller than the range
528 of foreshock occurrences, such that the aftershocks also migrate upward using several planes,
529 which can be appropriately explained by the pore pressure migration model in a consistent
530 manner. Thus, we prefer the hypothesis that states that the combined effects of pore pressure
531 migration and triggered aseismic slip are responsible for generating the 2017 M5.3 Kagoshima
532 Bay earthquake sequence.

533

534 **4.2. Upward migration of the aftershock activity along several planes**

535 Overall, we find that the aftershock hypocenters migrated toward the shallower portion
536 using several planes, which were dipping steeply to the east. Previous studies have also reported
537 such upward movements in the hypocenters for several earthquake swarms in northeastern Japan
538 induced by the M9.0 Tohoku-Oki earthquake (Okada et al., 2015; Yoshida & Hasegawa,
539 2018a,b). As these upward movements occurred in the stress shadow of the 2011 Tohoku-Oki
540 earthquake, these studies estimate the cause as upward pore pressure migration after the 2011
541 Tohoku-Oki earthquake (Terakawa et al., 2013; Yoshida et al., 2016a). The upward migration of
542 aftershocks within the present earthquake sequence can also be explained by the upward
543 migration of pore pressure. Fluid paths in the crust may have expanded due to the deformation
544 and shaking associated with the mainshock. This observation is similar to the prediction from the
545 fault valve model proposed in Sibson (1992), where fluids discharge upward after the mainshock
546 rupture.

547 Based on model simulations, Hainzl and Ogata (2005) point out that the background
548 seismicity rate of the ETAS model is sensitive to the amount of injected water. Pore pressure
549 migration may explain deviations in the seismicity rate from Omori's law in terms of the present
550 earthquake. Previous studies have obtained similar observations for fluid-injection-induced
551 seismicity and natural earthquake sequences (Llenos & Michael, 2013; Yoshida & Hasegawa,
552 2018b; Kumazawa et al., 2019). Hypocenters rapidly migrate upward during this period (Fig.
553 S7), supporting this hypothesis.

554

555 **4.3. Comprehensive interpretation of the seismic activity in Kagoshima Bay**

556 Here, we propose a simple model that comprehensively explains the observed results of
557 the foreshock-mainshock-aftershock sequence of the 2017 M5.3 Kagoshima Bay earthquake.
558 First, the foreshock activity represents the occurrence of small earthquakes caused by fluids that
559 have infiltrated the mainshock fault plane. We presume that the subducting slab is the source of
560 fluids, similar to the model reported in Hasegawa et al. (2005). The hypocenter migration of the
561 foreshock activity can be interpreted as a reflection of fluid movement and possibly triggered
562 aseismic slips on the plane.

563 Second, the seismic gap in the foreshock activity originates from the spatial
564 heterogeneities in the frictional and material properties along the fault plane. The fault strength
565 of the mainshock rupture area may have been higher than that of the surrounding area, as
566 proposed in the asperity model of Lay & Kanamori (1981). Alternatively, the area may have

567 been covered by an impermeable medium, such that fluid intrusion was difficult. Foreshocks
568 activities can be understood based on the failures of small seismogenic patches in the
569 surrounding area. The occurrence of foreshocks and possible aseismic slips increases the shear
570 stress at the future source region of the mainshock rupture. The mainshock rupture finally
571 occurred in this region due to the gradually increasing pore pressure and shear stress.

572 Third, the change in stress associated with the occurrence of the mainshock primarily
573 triggered the aftershocks in the area surrounding the mainshock rupture, including areas outside
574 the mainshock fault plane. Fluids also began to move upward due to the deformation and shaking
575 associated with the mainshock rupture. Together with the fluids, the aftershock hypocenters
576 moved from deep to shallow portions.

577 Thus, the overall sequence of the 2017 M5.3 Kagoshima Bay earthquake can be
578 appropriately explained by upward fluid movement, as presumed by the fault-valve model of
579 Sibson (1992).

580

581 5. Conclusions

582 We relocated the hypocenters of the earthquake sequence of the 2017 M5.3 Kagoshima
583 Bay earthquake based on the Double-Difference method (Waldhauser & Ellsworth, 2000) using
584 numerous and precise differential arrival time data. Relocated hypocenters show that most
585 earthquakes occurred on several planes. The orientations of those in the nodal planes of the focal
586 mechanisms for individual earthquakes are nearly parallel to those macroscopic planes in the
587 hypocenters, suggesting that these individual earthquakes occurred due to slip on several of these
588 planar structures.

589 Most foreshocks were located on a single plane steeply dipping to the east, with migration
590 along the plane. The observed speed and spatial pattern of hypocenter migration were consistent
591 with the pore pressure diffusion model ($D_h = 0.01\text{--}10\text{ m}^2/\text{s}$; e.g., Talwani et al. 2007; Shelly et
592 al., 2016; Yoshida & Hasegawa, 2018a). This suggests that fluid movement caused foreshock
593 activity and its migration behavior. Aseismic slip may have also been triggered by an increase in
594 the pore pressure and contributed to the foreshock occurrence.

595 Foreshocks hypocenters clearly formed a seismic gap in the middle of the foreshock
596 distribution, where the aftershock seismicity also appears to avoid this gap. The mainshock
597 hypocenter was located along an edge of this seismic gap. Furthermore, the source size of the
598 mainshock rupture estimated by the circular crack model was approximately the same as that of
599 the seismic gap. This suggests that the mainshock rupture was due to the slip of this seismic gap.
600 The seismic gap may be a large seismogenic patch with a relatively higher fault strength, which
601 finally ruptured due to pore pressure migration and possible aseismic slip in the surrounding
602 areas.

603 Aftershocks occurred on several planes, most of which have a steep incline to the east, and
604 moved, as a whole, from deeper to shallower portions. This can be explained by upward fluid
605 movement along all of the inclined planes after the mainshock. The overall sequence of the 2017
606 M5.3 Kagoshima Bay earthquake can be appropriately explained by upward fluid movement, as
607 presumed by the fault-valve model proposed in Sibson (1992).

609 Acknowledgments

610 This study used hypocenter and P- and S-wave arrival time data reported in the unified
611 catalog of the JMA (https://www.data.jma.go.jp/svd/eqev/data/bulletin/index_e.html). The
612 seismograms were collected and stored by the JMA, national universities, and National Research
613 Institute for Earth Science and Disaster Resilience (<http://www.hinet.bosai.go.jp/?LANG=en>).
614 The figures in this paper were created using GMT (Wessel & Smith, 1998). This research was
615 supported by JSPS KAKENHI Grant Number JP 17K1437. The obtained results for the
616 hypocenters, focal mechanisms, and coseismic slip distribution are available at
617 <http://www.aob.gp.tohoku.ac.jp/~yoshida/pub/JGR2020b/>.

618
619

620 **References**

- 621 Aki, K. (1965). A computer program for precise determination of focal mechanism of local
622 earthquakes by revising focal depths and crust-mantle structure. *Bull. Earthq. Res. Inst*, 43,
623 15–22.
- 624 Aki, K. (1967). Scaling law of seismic spectrum. *Journal of Geophysical Research*, 72(4), 1217–
625 1231.
- 626 Asano, Y., Saito, T., Ito, Y., Shiomi, K., Hirose, H., Matsumoto, T., et al. (2011). Spatial
627 distribution and focal mechanisms of aftershocks of the 2011 off the Pacific coast of
628 Tohoku Earthquake. *Earth, Planets and Space*, 63(7), 29.
- 629 Cornet, F. H., Helm, J., Poitrenaud, H., & Etchecopar, A. (1997). Seismic and aseismic slips
630 induced by large-scale fluid injections. In *Seismicity associated with mines, reservoirs and
631 fluid injections* (pp. 563–583). Springer.
- 632 Cox, S. F. (2016). Injection-driven swarm seismicity and permeability enhancement:
633 Implications for the dynamics of hydrothermal ore systems in high fluid-flux,
634 overpressured faulting regimes—An invited paper. *Economic Geology*, 111(3), 559–587.
- 635 Dahm, T. (1996). Relative moment tensor inversion based on ray theory: theory and synthetic
636 tests. *Geophysical Journal International*, 124(1), 245–257.
- 637 Das, S., & Henry, C. (2003). Spatial relation between main earthquake slip and its aftershock
638 distribution. *Reviews of Geophysics*, 41(3).
- 639 De Barros, L., Cappa, F., Deschamps, A., & Dublanchet, P. (2020). Imbricated Aseismic Slip
640 And Fluid Diffusion Drive A Seismic Swarm In The Corinth Gulf, Greece. *Geophysical
641 Research Letters*.
- 642 Dodge, D. A., Beroza, G. C., & Ellsworth, W. L. (1996). Detailed observations of California
643 foreshock sequences: Implications for the earthquake initiation process. *Journal of
644 Geophysical Research: Solid Earth*, 101(B10), 22371–22392.
- 645 Ebel, J. E., & Chambers, D. W. (2016). Using the locations of $M \geq 4$ earthquakes to delineate the
646 extents of the ruptures of past major earthquakes. *Geophysical Supplements to the
647 Monthly Notices of the Royal Astronomical Society*, 207(2), 862–875.
- 648 Ellsworth, W. L. (2013). Injection-induced earthquakes. *Science*, 341(6142), 1225942.
- 649 Guglielmi, Y., Cappa, F., Avouac, J.-P., Henry, P., & Ellsworth, D. (2015). Seismicity triggered
650 by fluid injection--induced aseismic slip. *Science*, 348(6240), 1224–1226.
- 651 Gutenberg, B., & Richter, C. F. (1944). Frequency of earthquakes in California. *Bulletin of the
652 Seismological Society of America*, 34(4), 185–188.
- 653 Hainzl, S., & Ogata, Y. (2005). Detecting fluid signals in seismicity data through statistical
654 earthquake modeling. *Journal of Geophysical Research: Solid Earth*, 110(5), 1–10.
655 <https://doi.org/10.1029/2004JB003247>
- 656 Hasegawa, A. (2017). Role of H₂O in Generating Subduction Zone Earthquakes. *Monographs on
657 Environment, Earth and Planets*, 5(1), 1–34.
658 <https://doi.org/10.5047/meep.2017.00501.0001>
- 659 Hasegawa, A., Nakajima, J., Umino, N., & Miura, S. (2005). Deep structure of the northeastern
660 Japan arc and its implications for crustal deformation and shallow seismic activity.
661 *Tectonophysics*, 403(1–4), 59–75. <https://doi.org/10.1016/j.tecto.2005.03.018>
- 662 Hubbert, M. K., & Rubey, W. W. (1959). Role of fluid overpressure in the mechanics of
663 overthrust faulting. *Geological Society of America Bulletin*, 70, 167–206.
664 [https://doi.org/10.1130/0016-7606\(1959\)70](https://doi.org/10.1130/0016-7606(1959)70)

- 665 Kato, A., Fukuda, J., Nakagawa, S., & Obara, K. (2016). Foreshock migration preceding the
666 2016 Mw 7.0 Kumamoto earthquake, Japan. *Geophysical Research Letters*, 43(17), 8945–
667 8953. <https://doi.org/10.1002/2016GL070079>
- 668 Kumazawa, T., & Ogata, Y. (2013). Quantitative description of induced seismic activity before
669 and after the 2011 Tohoku-Oki earthquake by nonstationary ETAS models. *Journal of*
670 *Geophysical Research: Solid Earth*, 118(12), 6165–6182.
- 671 Kumazawa, T., Ogata, Y., & Tsuruoka, H. (2019). Characteristics of seismic activity before and
672 after the 2018 M6.7 Hokkaido Eastern Iwate earthquake. *Earth, Planets and Space*, 71(1),
673 1–17.
- 674 Lay, T., & Kanamori, H. (1981). An asperity model of large earthquake sequences. In
675 *Earthquake Prediction. Maurice Ewing Series* (pp. 579–592). American Geophysical
676 Union.
- 677 Llenos, A. L., & Michael, A. J. (2013). Modeling earthquake rate changes in Oklahoma and
678 Arkansas: Possible Signatures of induced seismicity. *Bulletin of the Seismological Society*
679 *of America*, 103(5), 2850–2861. <https://doi.org/10.1785/0120130017>
- 680 Lohman, R. B., & McGuire, J. J. (2007). Earthquake swarms driven by aseismic creep in the
681 Salton Trough, California. *Journal of Geophysical Research: Solid Earth*.
682 <https://doi.org/10.1029/2006JB004596>
- 683 Madariaga, B. Y. R. (1976). Dynamics of an expanding circular fault. *Bulletin of the*
684 *Seismological Society of America*, 66, 639–666. [https://doi.org/10.1111/j.1461-](https://doi.org/10.1111/j.1461-0248.2009.01352.x)
685 [0248.2009.01352.x](https://doi.org/10.1111/j.1461-0248.2009.01352.x)
- 686 Mendoza, C., & Hartzell, S. H. (1988). Aftershock patterns and main shock faulting. *Bulletin of*
687 *the Seismological Society of America*, 78(4), 1438–1449.
- 688 Nanjo, K. Z., Miyaoka, K., Tamaribuchi, K., Kobayashi, A., & Yoshida, A. (2018). Related
689 spatio-temporal changes in hypocenters and the b value in the 2017 Kagoshima Bay
690 swarm activity indicating a rise of hot fluids. *Tectonophysics*, 749, 35–45.
- 691 Nur, A., & Booker, J. R. (1972). Aftershocks caused by pore fluid flow? *Science*, 175(4024),
692 885–887. <https://doi.org/10.1126/science.175.4024.885>
- 693 Ogata, Y. (2006). Statistical analysis of seismicity: updated version (SASeis2006). Institute of
694 Statistical Mathematics.
- 695 Ogata, Y. (1988). Statistical models for earthquake occurrences and residual analysis for point
696 processes. *Journal of the American Statistical Association*, 83(401), 9–27.
- 697 Okada, T., Matsuzawa, T., Umino, N., Yoshida, K., Hasegawa, A., Takahashi, H., et al. (2016).
698 Hypocenter migration and crustal seismic velocity distribution observed for the inland
699 earthquake swarms induced by the 2011 Tohoku-Oki earthquake in NE Japan:
700 Implications for crustal fluid distribution and crustal permeability. In *Crustal Permeability*
701 (pp. 307–323). <https://doi.org/10.1002/9781119166573.ch24>
- 702 Rice, J. R. (1992). Fault stress states, pore pressure distributions, and the weakness of the San
703 Andreas fault. In *International geophysics* (Vol. 51, pp. 475–503). Elsevier.
- 704 Roland, E., & McGuire, J. J. (2009). Earthquake swarms on transform faults. *Geophysical*
705 *Journal International*, 178(3), 1677–1690. [https://doi.org/10.1111/j.1365-](https://doi.org/10.1111/j.1365-246X.2009.04214.x)
706 [246X.2009.04214.x](https://doi.org/10.1111/j.1365-246X.2009.04214.x)
- 707 Ross, Z. E., Kanamori, H., & Hauksson, E. (2017). Anomalously large complete stress drop
708 during the 2016 Mw5.2 Borrego Springs earthquake inferred by waveform modeling and
709 near-source aftershock deficit. *Geophysical Research Letters*, 44(12), 5994–6001.
710 <https://doi.org/10.1002/2017GL073338>

- 711 Ross, Z. E., Kanamori, H., Hauksson, E., & Aso, N. (2018). Dissipative Intraplate Faulting
712 During the 2016 Mw6.2 Tottori, Japan Earthquake. *Journal of Geophysical Research:*
713 *Solid Earth*, 123(2), 1631–1642. <https://doi.org/10.1002/2017JB015077>
- 714 Ross, Z. E., Rollins, C., Cochran, E. S., Hauksson, E., Avouac, J. P., & Ben-Zion, Y. (2017).
715 Aftershocks driven by afterslip and fluid pressure sweeping through a fault-fracture mesh.
716 *Geophysical Research Letters*, 44(16), 8260–8267. <https://doi.org/10.1002/2017GL074634>
- 717 Saiga, A., Matsumoto, S., Uehira, K., Matsushima, T., & Shimizu, H. (2010). Velocity structure
718 in the crust beneath the Kyushu area. *Earth, Planets and Space*, 62(5), 449–462.
- 719 Sato, T., & Hirasawa, T. (1973). Body wave spectra from propagating shear cracks. *Journal of*
720 *Physics of the Earth*, 21(4), 415–431. <https://doi.org/10.4294/jpe1952.21.415>
- 721 Scholz, C. H. (1998). Earthquakes and friction laws. *Nature*, 391(6662), 37–42.
722 <https://doi.org/10.1038/34097>
- 723 Shapiro, S. A., Huenges, E., & Borm, G. (1997). Estimating the crust permeability from fluid-
724 injection-induced seismic emission at the KTB site. *Geophysical Journal International*,
725 131(2). <https://doi.org/10.1111/j.1365-246X.1997.tb01215.x>
- 726 Shelly, D. R., Ellsworth, W. L., & Hill, D. P. (2016). Fluid-faulting evolution in high definition:
727 Connecting fault structure and frequency-magnitude variations during the 2014 Long
728 Valley Caldera, California, earthquake swarm. *Journal of Geophysical Research : Solid*
729 *Earth*, 121, 1776–1795. <https://doi.org/10.1002/2015JB012719>.Received
- 730 Sibson, R. H. (2020). Preparation zones for large crustal earthquakes consequent on fault-valve
731 action. *Earth, Planets and Space*, 72(1), 1–20.
- 732 Talwani, P., & Acree, S. (1985). Pore pressure diffusion and the mechanism of reservoir-induced
733 seismicity. In *Earthquake Prediction* (pp. 947–965). Springer.
- 734 Talwani, P., Chen, L., & Gahalaut, K. (2007). Seismogenic permeability, ks. *Journal of*
735 *Geophysical Research: Solid Earth*, 112(7), 1–18. <https://doi.org/10.1029/2006JB004665>
- 736 Terakawa, T., Hashimoto, C., & Matsu'ura, M. (2013). Changes in seismic activity following the
737 2011 Tohoku-oki earthquake: Effects of pore fluid pressure. *Earth and Planetary Science*
738 *Letters*, 365, 17–24. <https://doi.org/10.1016/j.epsl.2013.01.017>
- 739 Ueno, H., Hatakeyama, S., Aketagawa, T., Funasaki, J., & Hamada, N. (2002). Improvement of
740 hypocenter determination procedures in the Japan Meteorological Agency. *Q. J. Seismol.*,
741 65, 123–134.
- 742 Utsu, T. (1961). A statistical study on the occurrence of aftershocks. *Geophys. Mag.*, 30, 521–
743 605.
- 744 Utsu, T., Ogata, Y., & Matsu'ura, R. (1995). The centenary of the Omori formula for a decay law
745 of aftershock activity. *Journal of Physics of the Earth*, 43(1), 1–33.
- 746 Vidale, J. E., Boyle, K. L., & Shearer, P. M. (2006). Crustal earthquake bursts in California and
747 Japan: Their patterns and relation to volcanoes. *Geophysical Research Letters*, 33(20), 1–
748 5. <https://doi.org/10.1029/2006GL027723>
- 749 Waite, G. P., & Smith, R. B. (2002). Seismic evidence for fluid migration accompanying
750 subsidence of the Yellowstone caldera. *Journal of Geophysical Research: Solid Earth*,
751 107(B9), ESE--1.
- 752 Waldhauser, F. (2002). Fault structure and mechanics of the Hayward Fault, California, from
753 double-difference earthquake locations. *Journal of Geophysical Research*, 107(B3), 2054.
754 <https://doi.org/10.1029/2000JB000084>

- 755 Wetzler, N., Lay, T., Brodsky, E. E., & Kanamori, H. (2018). Systematic deficiency of
756 aftershocks in areas of high coseismic slip for large subduction zone earthquakes. *Science*
757 *Advances*, 4(2), 1–10. <https://doi.org/10.1126/sciadv.aao3225>
- 758 Woessner, J., Schorlemmer, D., Wiemer, S., & Mai, P. M. (2006). Spatial correlation of
759 aftershock locations and on-fault main shock properties. *Journal of Geophysical Research:*
760 *Solid Earth*, 111(B8).
- 761 Yabe, S., & Ide, S. (2018). Variations in precursory slip behavior resulting from frictional
762 heterogeneity. *Progress in Earth and Planetary Science*, 5(1), 43.
- 763 Yoshida, K., & Hasegawa, A. (2018a). Sendai-Okura earthquake swarm induced by the 2011
764 Tohoku-Oki earthquake in the stress shadow of NE Japan: Detailed fault structure and
765 hypocenter migration. *Tectonophysics*, 733(August 2017), 132–147.
766 <https://doi.org/10.1016/j.tecto.2017.12.031>
- 767 Yoshida, K., & Hasegawa, A. (2018b). Hypocenter Migration and Seismicity Pattern Change in
768 the Yamagata-Fukushima Border, NE Japan, Caused by Fluid Movement and Pore
769 Pressure Variation. *Journal of Geophysical Research: Solid Earth*, 123(6), 5000–5017.
770 <https://doi.org/10.1029/2018JB015468>
- 771 Yoshida, K., Hasegawa, A., & Okada, T. (2016a). Heterogeneous stress field in the source area
772 of the 2003 M6.4 Northern Miyagi Prefecture, NE Japan, earthquake. *Geophysical Journal*
773 *International*, 206(1), 408–419. <https://doi.org/10.1093/gji/ggw160>
- 774 Yoshida, K., Hasegawa, A., & Yoshida, T. (2016b). Temporal variation of frictional strength in
775 an earthquake swarm in NE Japan caused by fluid migration. *Journal of Geophysical*
776 *Research: Solid Earth*, 121(8), 5953–5965. <https://doi.org/10.1002/2016JB013022>
- 777 Yoshida, K., Hasegawa, A., Yoshida, T., & Matsuzawa, T. (2019a). Heterogeneities in stress and
778 strength in tohoku and its relationship with earthquake sequences triggered by the 2011
779 M9 Tohoku-Oki earthquake. *Pure and Applied Geophysics*, 176(3), 1335–1355.
- 780 Yoshida, K., Saito, T., Emoto, K., Urata, Y., & Sato, D. (2019b). Rupture directivity, stress
781 drop, and hypocenter migration of small- and moderate-sized earthquakes in the
782 Yamagata-Fukushima border swarm triggered by upward pore-pressure migration after the
783 2011 Tohoku-Oki earthquake. *Tectonophysics*, 769, 228184.
- 784 Yoshida, K., Taira, T., Matsumoto, Y., Saito, T., Emoto, K., & Matsuzawa, T. (n.d.). Stress
785 release process along an intraplate fault analogous to the plate boundary: a case study of
786 the 2017 M5. 2 Akita-Daisen earthquake, NE Japan. *Journal of Geophysical Research:*
787 *Solid Earth*, e2020JB019527.
- 788 Yukutake, Y., Ito, H., Honda, R., Harada, M., Tanada, T., & Yoshida, A. (2011). Fluid-induced
789 swarm earthquake sequence revealed by precisely determined hypocenters and focal
790 mechanisms in the 2009 activity at Hakone volcano, Japan. *Journal of Geophysical*
791 *Research: Solid Earth*, 116(4). <https://doi.org/10.1029/2010JB008036>